Processing of Ceramic Blocks Using Femtosecond Lasers

Noritsugu KITAO, Eiichi MATSUBARA, Kazutoshi KAKIMOTO,
Toru TSUJIBAYASHI and Yutaka KOMASA

Reprinted from Journal of Japanese Society of Laser Dentistry

Vol. 27, No 3 December 2016

日レ歯誌 J. Jpn. Soc. Laser Dent. 27：90-100, 2016

Processing of Ceramic Blocks Using Femtosecond Lasers

Noritsugu KITAO[1], Eiichi MATSUBARA[2], Kazutoshi KAKIMOTO[3], Toru TSUJIBAYASHI[2] and Yutaka KOMASA[3]

[1] Department of Graduate School of Dentistry (Geriatric Dentistry)
[2] Department of Physics, Osaka Dental University
[3] Department of Geriatric Dentistry, Osaka Dental University

(Received: September 14, 2016, Accepted for Publication: November 28, 2016)

フェムト秒レーザーを用いたセラミックブロックの切削

北尾徳嗣[1] 松原英一[2] 柿本和俊[3]
辻林徹[2] 小正裕[3]

[1] 大阪歯科大学大学院歯学研究科（高齢者歯科学専攻）
[2] 大阪歯科大学物理学教室
[3] 大阪歯科大学高齢者歯科学講座

（受付：2016年9月14日，受理：2016年11月28日）

要旨：フェムト秒レーザーを用いたセラミックブロックの切削について検討した。実験材料には，完全焼結ジルコニア，半焼結ジルコニア，アルミナおよびハイドロキシアパタイトを用いた。設定条件は波長，照射光強度，焦点外し距離，オートステージの移動速度および切削粉除去のためのエアーの有無とし，設定条件を変化させてレーザー照射して形成した切削痕の深さと断面積を比較した。

その結果，材料内部に水が浸透すると切削力が増した。ジルコニアは黒化が見られたが，再加熱で消失した。切削力は照射光強度に依存性があった。照射光強度が増加すると切削痕の深さと断面積は増加したが，20mWを超えると増加量は低下した。同じ照射光強度では，波長は短い方，パルス幅は短い方が切削量は大きかった。切削粉の除去が切削に有効であった。窩洞形成した窩底の表面粗さは，臨床応用可能な範囲であった。

以上から，フェムト秒チタンサファイアレーザーは歯科用セラミックの高精度な加工に応用できることが示唆された。

(J. Jpn. Soc. Laser Dent. 27：90～100, 2016 Reprint requests to Dr. KITAO)

Key words＝Femtosecond laser, Ceramic, Zirconia, Processing

キーワード＝フェムト秒レーザー，セラミック，ジルコニア，加工

Introduction

Recently, ceramics has rapidly gained in popularity among dental restorative materials[1] because of increased desire for aesthetics, improvements in materials, and development of computer aided design/computer aided manufacturing (CAD/CAM) systems. Zirconia is the most frequently used material for all-ceramic crowns owing to its overwhelmingly high fracture toughness[2-3]. Zirconia crowns are processed either by cutting completely-sintered materials with a cutting tool, or by cutting semi-sintered crowns and then completely sintering. Although the former method yields better processing precision, the latter is widely adopted because of its ease.

To process completely sintered zirconia, the use of a laser instead of a mechanical cutting tool has been considered, and processing using a pulsed nanosecond Nd:YVO_4 laser has been reported[4]. However, the pro-

〒573-1121 大阪府枚方市楠葉花園町8-1 TEL 072-864-3074 FAX 072-864-3174
8-1 Kuzuhahanazono-cho, Hirakata-shi, Osaka 573-1121, Japan. TEL +81-72-864-3074 FAX +81-72-864-3174

cessing precision still has room for improvement compared to that in processing semi-sintered zirconia with mechanical cutting tool[5-15]. Femtosecond lasers with pulse widths shorter than nano- and picosecond, are used in a wide range of applications including medical surgery[16, 17]. In the field of dentistry, there have been a few reports regarding the cutting of hard dental tissue using femtosecond lasers[18-20]. However, owing to the lack of practical method for guiding light within an oral cavity without losing laser energy, and safety concerns, there are limits on the output power and wavelength range that can be used, so that nothing has been found that is superior to the Er:YAG laser already used for clinical applications. On the other hand, there have been practically no reports pertaining to the preparation of dental prosthetic devices using femtosecond lasers. In the present study, we considered whether an all-ceramic crown could be processed by using a femtosecond laser on dental prosthetic appliances for which high precision processing is required.

Alumina ranks with zirconia as a material for restorative materials owing to its prominent mechanical properties. Hydroxyapatite has excellent biocompatibility and has been studied as a possible new prosthetic material. Although hydroxyapatite has not been used for dental prostheses because of the difficulty in processing, and insufficient Vickers hardness and bending strength[21, 22], hydroxyapatite coatings have been put into practical use for implants in recent years[23]. Research and development on apatite sheets for dentin restoration have also been conducted[24, 25]. The Vickers hardness of hydroxyapatite complex has also increased[21, 22], so it is expected that hydroxyapatite will be put to practical use in the future.

Accordingly, the objective of the present study is to seek a new method for processing all-ceramic crowns containing alumina and hydroxyapatite, in addition to zirconia.

Experimental materials and procedures

1. Experimental materials

The zirconia samples were either completely-sintered yttria-stabilized zirconia blocks (Y-TZP Z-CAD®, TKT METOXIT AG, Thayngen), henceforth referred to as Y-TZP, or semi-sintered yttria-stabilized zirconia blocks (Y-TZP Z-CAD®, TKT METOXIT AG), henceforth referred to as Semi-Y-TZP. The alumina samples were completely-sintered alumina blocks (CHEMISTON Co., Ltd., Saitama), henceforth referred to as Al_2O_3. The hydroxyapatite samples were either dense $Ca_{10}(PO_4)_6(OH)_2$ (CELLYARD pellet®, HOYA Co., Ltd., Tokyo), henceforth referred to as HAP100, or porous $Ca_{10}(PO_4)_6(OH)_2$ (CELLYARD HA scaffold®, HOYA Co., Ltd.), henceforth referred to as HAP50.

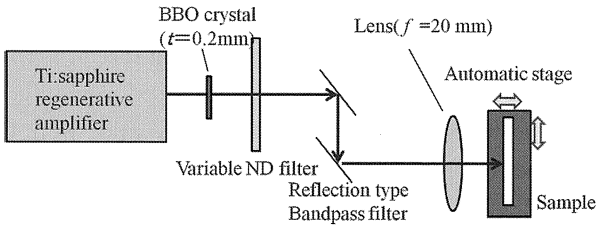

Figure 1 Experimental setup for processing ceramic samples

Alumina and hydroxyapatite were used only to compare materials and the presence or absence of water, and subsequent experiments were carried out only with the zirconia most commonly used for all-ceramic crowns.

2. Laser equipment

The following laser systems were used in the experiments.

- A femtosecond Ti:sapphire regenerative amplifier laser system (central wavelength $\lambda = 800$nm, pulse width $\tau_p = 50$fs, and 1kHz repetition rate)
- A femtosecond Ti:sapphire regenerative amplifier laser system (central wavelength $\lambda = 800$nm, pulse width $\tau_p = 150$fs, and 1kHz repetition rate)

3. Optical path

Figure 1 shows a schematic diagram of the optical path. The output beam of the regenerative amplifier passed through a 0.2mm thick β-BaB_2O_4 (BBO) crystal and generated a second harmonic with a central wavelength of 400nm. When performing 400nm irradiation experiments, the light was passed through a reflection-type bandpass filter to cut out the fundamental 800nm component. In 800nm irradiation experiments, the angle of the BBO crystal was adjusted so as not to produce a second harmonic, and the beam was similarly passed through an 800nm reflection-type bandpass filter. The laser light intensity was attenuated using a variable Neutral Density filter (ND filter), and the beam was focused using a synthetic quartz lens (focal length 20mm). We attached three actuators (Optmike-E, SIGMAKOKI Co., Ltd., Saitama) to a manual XYZ stage and used it as an automatic stage. The sample was mounted vertically on

an automatic stage, and the laser pulses irradiated the sample at normal incidence at a repetition rate of 1kHz.

4. Experimental conditions

The experimental conditions that were varied were the wavelength, irradiation power, defocus distance, automatic stage movement speed, and whether or not there was an air flow for removing debris. The central wavelength of the irradiating light pulses was set to either 800 or 400nm. The light intensity following the bandpass filter was measured using a power meter (PS19, Coherent, Inc., Santa Clara).

Figure 2 shows a schematic diagram of the relationship between the lens focal point and the sample. The focal point was at the center of the plasma generated by ionization of air molecules, where the light power is set as low as possible in the condition that the plasma could be visually observed. As seen in Figure 2, the defocus distance was taken to be negative when the sample was on the lens side of the focal point, and positive when on the opposite side.

The automatic stage movement speed could be adjusted in the range of 1 to 100μm/s.

5. Experimental procedure

Samples were mounted on the automatic stage, and were irradiated at normal incidence with laser pulses at a 1kHz repetition rate. The depth and sectional area of the irradiation traces on the sample surface were measured using a 3CCD real color confocal microscope (H1200, Lasertec Corporation, Kanagawa), henceforth referred to as confocal microscope. These measurements were performed at 10 random locations, and the results were averaged.

1) Effect of defocus distance

To determine the effect of the defocus distance on the depth and sectional area of the irradiation traces, the dry Y-TZP samples were used. The laser wavelength was 400nm, the pulse width was 50fs, the irradiation power was 20mW, the sample movement speed was 100μm/s, and the defocus distance was varied from −400 to +200μm in 50μm increments. We examined this dependence because we found the processing efficiency significantly depended on the defocus distance in early stage of our research. In addition, there was uncertainty of ± 100μm in the position of a sample with respect to the focal point. Hence, we also measured the defocus distance dependence in other experiments, so that we could always evaluate other dependences, excluding the influence of defocus distances.

2) Effect of type of material and presence of water

To determine the effect of type of material and presence of water on the depth and sectional area of the irradiation traces, dry and wet samples of HAP100, HAP50, Y-TZP, and Semi-Y-TZP Al_2O_3 were used. All samples were prepared two types of dry and wet. Wet types of

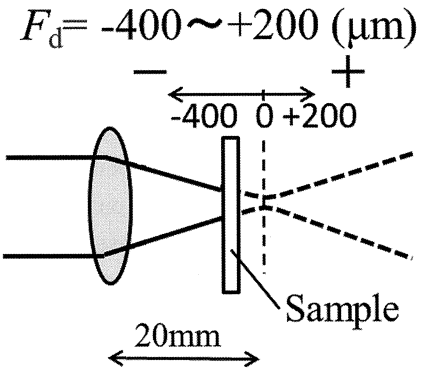

Figure 2 Position relations schematic view of defocused distance: F_d

Table 1 The exprimental conditions

Experiment	Conditions
1) Effect of defocus distance	From − 400 to + 200μm in 50μm increments
2) Effect of type of material and presence of water	Dry or wet samples of Y-TZP, semi Y-TZP, Al_2O_3, HAP100, HAP50
3) Effect of irradiation power	From 8 to 100 (8, 10, 20, 40, 60, 100) mW
4) Effect of laser wavelength and pulse width	Wavelength: 400nm (pulse width: 50fs) Wavelength: 800nm (pulse width: 50fs, 150fs)
5) Effect of sample movement speed and debris removal	Sample movement speed from 26 to 100 (26, 46, 67, 85, 100) μm/s With and without air folw during processing

all of these samples were also produced by soaking for one week in water. The laser wavelength was 400nm, the pulse width was 50fs, the irradiation power was 20mW, the sample movement speed was 100μm/s, and the defocus distance was varied from −400 to +200μm in 50μm increments. The surface of the irradiation traces was compared by naked eye observations and using scanning electron microscope (JSM-6500, JEOL Ltd., Tokyo, Japan). Then we investigated the dependence of the maximum depth and maximum sectional area of the irradiation trace at the defocus distance and on the presence or absence of water for each sample. An overall difference between the groups was tested by one-way analysis of variance for all of the experimental groups. Differences between groups were tested by a two-way analysis of variance for differences in materials and presence or absence of water, followed by a Tukey-Kramer's multiple-comparison post hoc test.

3) Effect of irradiation power

To determine the effect of the irradiation power on the depth and sectional area of the irradiation traces, the dry Y-TZP samples were used. The pulse width was 50fs, the defocus distance was −200μm, and the sample movement speed was 100μm/s. The laser wavelength was either 400 or 800nm, and the irradiation power was varied from 8 to 100 (8, 10, 20, 40, 60, 80 or 100) mW.

4) Effect of laser wavelength and pulse width

To determine the effect of laser wavelength and pulse width on the depth and sectional area of the irradiation traces, the dry Y-TZP samples were used. The irradiation power was 20mW, the sample movement speed was 100μm/s, the laser wavelength was 400 or 800nm, the pulse width was 50 or 150fs, and the defocus distance was varied from −400 to +200μm in 50μm increments. Then we investigated the dependence of the depth and sectional area of the irradiation trace on the wavelength and duration of femtosecond laser pulses for each defocus distance. Differences between groups were tested by a two-way analysis of variance for differences in the wavelength and pulse width, followed by a Tukey-Kramer's multiple-comparison post hoc test.

5) Effect of sample movement speed and debris removal

To determine the effect of sample movement speed and debris removal, on the depth and sectional area of the irradiation traces, the dry Y-TZP samples were used. The wavelength was 400nm, the pulse width was 50fs, the irradiation power was 20mW, and the defocus distance was −200μm. The sample movement speed was 26, 46, 67, 85, or 100μm/s, and irradiation was performed either with or without an air flow to remove the debris. The flow quantity of the air was approximately 10 liters a minute. Regression analysis was done by simple regression on the sample movement speed and the size of the irradiation trace.

6) Evaluation of cavity formation

Using a dry Y-TZP sample, a 1000μm long, 1000μm wide, and 300μm deep cavity was formed by laser irradiation. The laser wavelength was 800nm, the pulse width was 150fs, the irradiation power was 100mW, the defocus distance was −200μm, and the sample movement speed was 100μm/s. First we moved the sample along the x-axis of the automatic stage. Then we shifted the sample along the y-axis by 25μm, and moved along the x-axis again. We repeated this procedure until a two-dimensional trace with a size of 1000×1000μm was formed on the xy plane. Then we moved the sample along the direction of depth (z-axis) by 50μm and repeated the processing on the xy plane. After we irradiation sample, using a confocal microscope, the depth and surface roughness at 10 arbitrary locations on the cavity floor were measured. In addition, the time required for cavity formation was measured.

Experimental conditions and parameters are summarized in Table 1. All the experiments except experiment 3) were repeated three times for each condition.

Results

1) Effect of defocus distance

Figure 3 shows the relationship between the defocus distance and the depth and sectional area of the irradiation traces. It can be seen that the milled amount is the largest for a defocus distance of −300μm, and decreases away from this position. The defocus distance that led to the largest amount of processing was also found to be negative (sample on the lens side of the focal point) and this behavior did not depend on material or its conditions.

2) Effect of type of material and presence of water

Figure 4 compares the maximum values of the depth and sectional area for dry and wet samples of different materials. It can be seen that for the porous Semi-Y-TZP and HAP50 samples, the maximum values increased by a factor of two times or more, although the standard

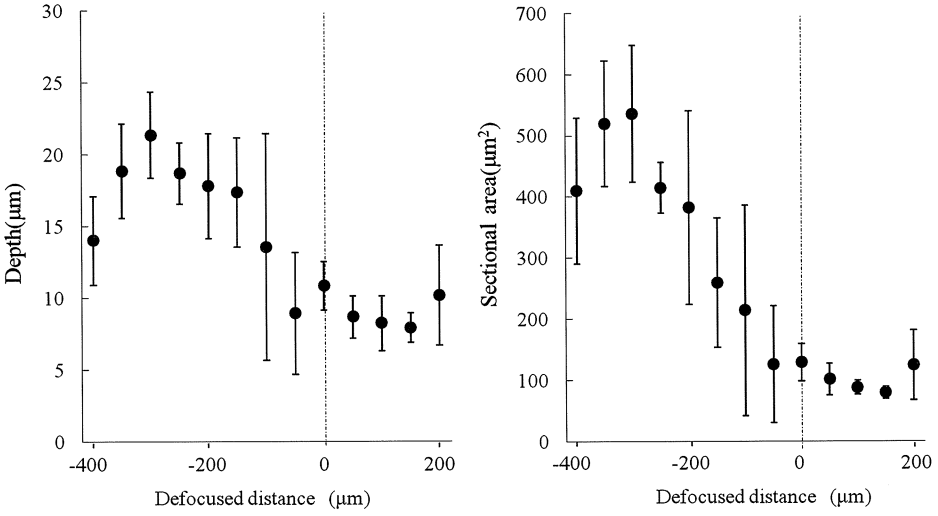

Sample Y-TZP DRY, Wave length 400 nm, Pulse widths 50 fs, Irradiation power 20 mW, Sample movement speed 100 μm/s (n=3)

Figure 3 The relationship between the defocus distance and the depth and sectional area of the irradiation traces

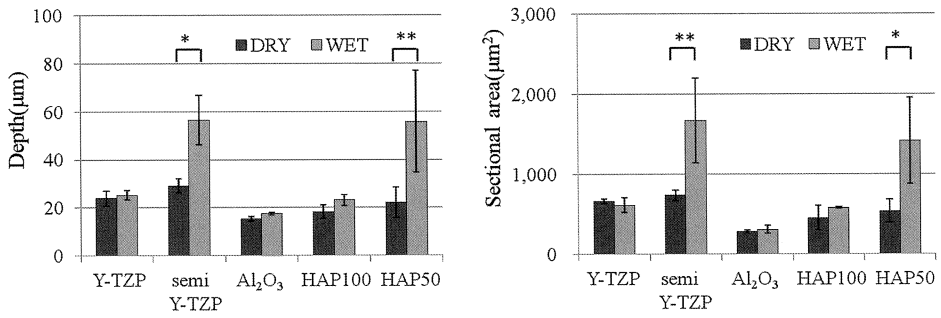

Wave length 400 nm, Pulse widths 50 fs, Irradiation power 20 mW, Sample movement speed 100 μm/s (n=3, ** p<0.01, * p<0.05 : Tukey-Kramer test after two-way ANOVA)

Figure 4 Comparison by each material with dry and wet (the maximum values of depth and sectional area)

deviation also became larger. A one-way analysis of variance for all of these samples indicated a significant effect of the experimental conditions on the irradiation trace depth ($p < 0.0001$) and sectional area ($p < 0.0001$). In addition, a Tukey-Kramer multiple comparison showed a significant effect of the presence of water for Semi-Y-TZP and HAP50, with a confidence level of greater than 95%. A two-way analysis of variance for the dense Y-TZP, HAP100, and Al_2O_3 samples revealed that there was a significant effect of the type of material ($p = 0.0002$) and the presence of water ($p = 0.0226$) on the depth of the irradiation trace. However, only the type of material had a significant ($p = 0.0001$) effect on the sectional area. A Tukey-Kramer multiple comparison showed that the largest amount of processing occurred for Y-TZP, followed by HAP100, and the sample that was hardest to mill was Al_2O_3. Furthermore, the irradiation trace became significantly larger when water was present.

Figure 5 presents photographs of irradiation traces on the sample surfaces. The traces appear black on the Y-TZP surface, and bluish-black on the Semi-T-TZP surface, but no such darkening appears on the HAP100, HAP50, or Al_2O_3 surface. The temperature of the Y-TZP and Semi Y-TZP samples was subsequently raised to 1,000℃ in air over the course of an hour, and then to 1,450℃ over the course of another hour. After sintering for two hours at 1,450℃ and cooling over the course of 30 min to 980℃, the darkening disappeared.

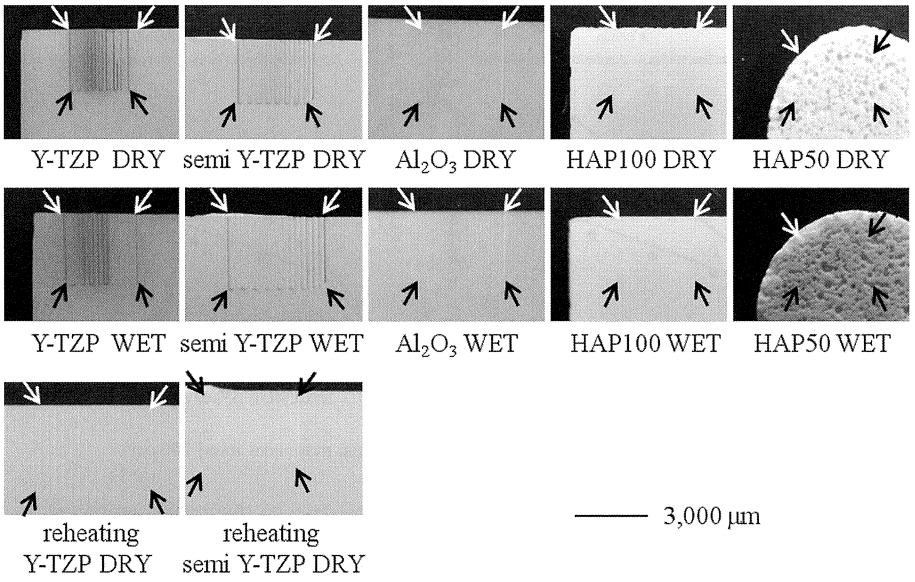

Figure 5 Observation photograph of the laser irradiation trace of the sample surface
The irradiation range is indicated by an arrow.

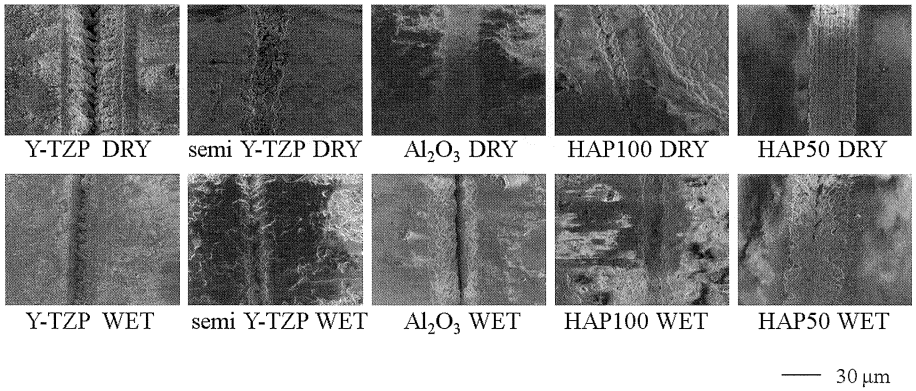

Figure 6 SEM photograph of the laser irradiation trace of the sample surface

Figure 6 shows SEM images of the irradiation traces on the different samples. For the dry Y-TZP sample, the edge of the trace is straight and distinct, and a rounded scales-like structure can be seen in the interior of the trace. For the wet Y-TZP sample, although the trace edge is straight, it is less distinct than that for the dry sample. A rounded scales-like structure again appears in the interior. For the dry Semi-Y-TZP sample, the trace edge is indistinct, and plate-like structures can be seen in the interior. The wet Semi-Y-TZP sample also exhibits an indistinct trace, but it contains a scales-like structure. For the dry HAP100 sample, the trace edge is straight and distinct, and an angular structure appears in the interior. Similar results are seen for the wet HAP100 sample, although the angular structure is more rounded. For the dry HAP50 sample, the trace edge is indistinct, and an angular scales-like structure appears in the interior. For the wet HAP50 sample, the trace edge is indistinct, and an angular structure appears in the interior. For the dry Al_2O_3 sample, the trace edge is straight, and a rounded scales-like structure appears in the interior. For the wet Al_2O_3 sample, the trace edge is straight, and a more rounded scales-like structure appears in the interior. In general, for all samples, the trace edges were somewhat more distinct for the dry samples.

3) Effect of irradiation power

Figure 7 shows the dependence of the trace depth and sectional area on the irradiation power. It can be seen that both the depth and sectional area increase rapidly

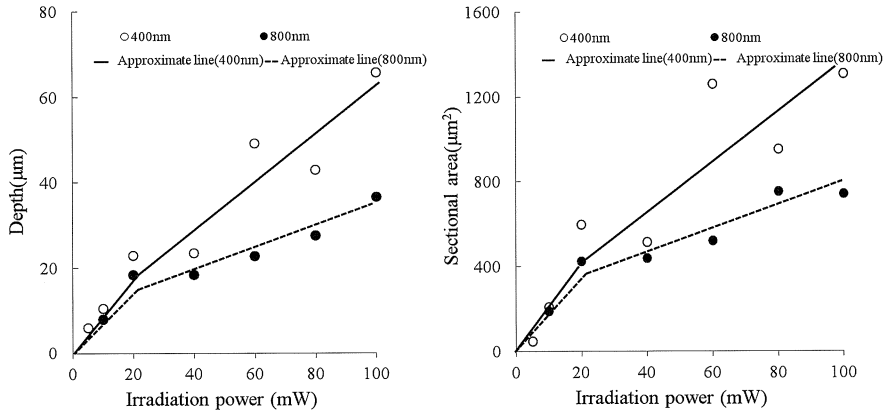

Sample Y-TZP DRY, Pulse widths 50 fs, F_d-200 μm, Sample movement speed 100 μm/s
(n=1)

Figure 7 Dependence of the trace depth and sectional area on the irradiation power

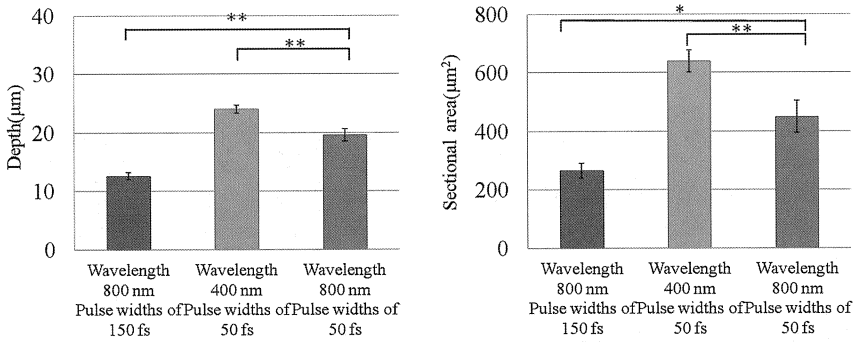

Sample Y-TZP DRY, Irradiation power 20 mW, Sample movement speed 100 μm/s
(n=3, ** p<0.01, * p<0.05: Tukey-Kramer test after two-way ANOVA)

Figure 8 Dependence of the maximum trace depth and sectional area on the wavelength and pulse width

up to 20mW, and then more slowly. Although the irradiation trace was seen at wavelength 800nm and irradiation power 8mW, it could not be measured with a confocal microscope.

4) Effect of laser wavelength and pulse width

Figure 8 shows the dependence of the maximum trace depth and sectional area on the wavelength and pulse width. A one-way analysis of variance showed a statistically significant (p<0.0001) effect of both the wavelength and pulse width. In addition, a Tukey-Kramer test identified a significant difference (p=0.0037) between wavelengths of 400 and 800nm, and also (p=0.0003) between pulse widths of 50 and 150fs at a wavelength of 800nm.

5) Effect of sample movement speed and debris removal

Figure 9 shows the dependence of the irradiation trace depth and sectional area on the sample movement speed and the presence or absence of an air flow to remove debris. When an air flow is present, both the depth and sectional area decrease with increasing movement speed, which is not the case without an air flow. In addition, although the trace depth and sectional area are larger in the presence of an air flow, the difference becomes smaller as the movement speed increases. Although a linear regression analysis of the data in Figure 9 gave negative regression coefficients for the groups both with and without air flow, the results were not statistically significant.

6) Evaluation of cavity formation

The average cavity depth was measured to be 308.2 ± 11.4μm, the average difference in cavity floor depth (R_{max}) was 37.5 ± 6.8μm, and the average roughness (R_a) was 4.5 ± 1.5μm. The processing time was 4.5h.

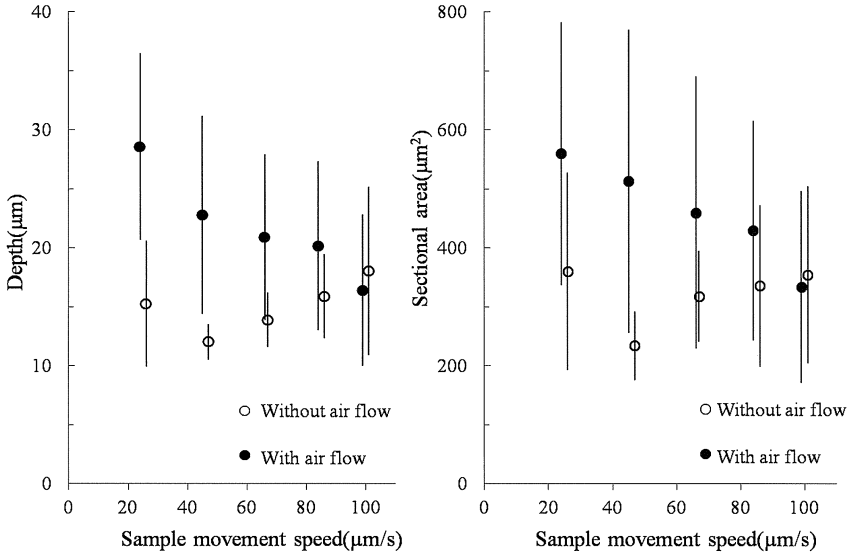

Sample Y-TZP DRY, Wave length 400 nm, Pulse widths 50 fs, F_d -200 μm, Irradiation power 20 mW (n=3)

Figure 9 Dependence of the irradiation trace depth and sectional area on the sample movement speed and the presence or absence of an air flow to remove debris

Discussion

1) Effect of defocus distance

The maximum amount of processing occurred at a defocus distance of approximately 300μm, that is, approximately 300μm from the focal point on the lens side, and it decreased further from this position. This is contrary to the expectation that the largest amount of processing would occur at the focal point, where the power density is at a maximum. This is thought to be due to the formation of a plasma in the air at the focal point because of the high laser light concentration. This plasma absorbs the laser light, causing the milling efficiency to decrease[26, 27].

2) Effect of type of material and presence of water

The large differences between the dry and wet cases for the Semi-Y-TZP and HAP50 samples are thought to be due to the presence of pores in these materials. Since Y-TZP, HAP100, and Al_2O_3 are dense, water cannot infiltrate into their interior. On the other hand, because HAP50 is porous hydroxyapatite, and Semi-Y-TZP is partially sintered zirconia, they do not have a dense interior, and moisture can infiltrate. This is thought to lead to enhanced processing as a result of explosive expansion of internal water that becomes vaporized due to laser heating. This suggests that if a porous Y-TZP material was developed[28], processing could be performed in a short period of time. On the other hand, because of the high standard deviation, that is, the large amount of variability, it will be necessary to investigate the precision with regard to porous materials.

From the photographs in Figure 5, the irradiation traces appeared black only for Y-TZP and Semi-Y-TZP; this therefore seems to be a particular characteristic of zirconia. Two causes for this darkening are considered: adhesion of ultrafine particles produced by the plasma generated by laser irradiation, and formation of oxygen-deficient zirconia (ZrO_{2-X}). Yoshioka et al. reported that darkening and cracking were observed when irradiating zirconia with a Q-switched Nd:YAG laser, that the cause for this was oxygen deficiency, and that the dark regions disappeared upon resintering[29]. Ban et al. also reported that darkening occurred when irradiating the surface of zirconia with a Nd:YAG laser, that its cause was oxygen deficiency due to laser heating, and that it disappeared upon resintering[30-33]. Since, in the present study, similar behavior was found for Y-TZP and Semi-Y-TZP, it can be concluded that the observed darkening is also the result of oxygen deficiency due to the heating induced by the laser.

The processing mechanism is considered from the viewpoint of laser ablation. When a laser irradiates a solid and the beam intensity exceeds a threshold value, the solid undergoes electronic, thermal, photochemical, and

physical changes, and its surface becomes etched. Laser ablation is classified into the categories of photothermal, photomechanical, and photochemical ablation[34, 35]. Photothermal ablation is a milling mechanism resulting from boiling or vaporization of internal water, and frequently produces a heat-affected zone. Photomechanical ablation is generated by short-pulse laser irradiation and it can produce a very thin heat-affected zone. In photochemical ablation, molecular bonds are severed by an ultraviolet laser or the high-energy photons associated with the blue-violet region of the spectrum, and it gives rise to very little scattering[34, 35].

When processing inorganic materials, photomechanical ablation and photochemical ablation are believed to occur. The oxygen deficiency that is thought to be the cause of the darkening described earlier is also believed to occur due to photochemical ablation. From the SEM images, because the trace edges for Y-TZP, HAP100, and Al_2O_3 were flat and did not have a thermally coagulated appearance, it is believed that mainly photomechanical ablation and photochemical ablation had occurred. Although the trace edges for Semi-Y-TZP and HAP50 were irregular had a stripped-away appearance, because of the absence of a thermally coagulated appearance, and from the sample shape, moisture had infiltrated the interior, it is believed that photothermal ablation combined with photomechanical ablation and photochemical ablation to increase the cutting force.

3) Effect of irradiation power

Both the irradiation trace depth and sectional area were found to increase with increasing light intensity, but the rate of increase was lower for an irradiation power above 20mW. This is thought to be because the laser beam is absorbed by plasma generated at high beam intensities, thus reducing the power density available for processing[26, 27].

4) Effect of laser wavelength and pulse width

The absorption edge (bandgap) for all of the materials in the present study is in the ultraviolet region, and the samples absorb light by multiphoton absorption. The significant difference in the maximum trace depth and sectional area for wavelengths of 400 and 800nm is thought to be because less absorption occurs at the shorter wavelength, and the multiphoton absorption efficiency increases. Furthermore, in these experiments, in order to keep the light intensity constant, when the same pulse energy is used, the number of photons contained in a 400nm light pulse is half that for an 800nm light pulse. In addition, broadening due to group velocity dispersion of the pulse used for focusing is greater with the 400nm pulse. Nevertheless, a higher processing rate was observed in the present study at a wavelength of 400nm, which suggests the superiority of shorter wavelength light.

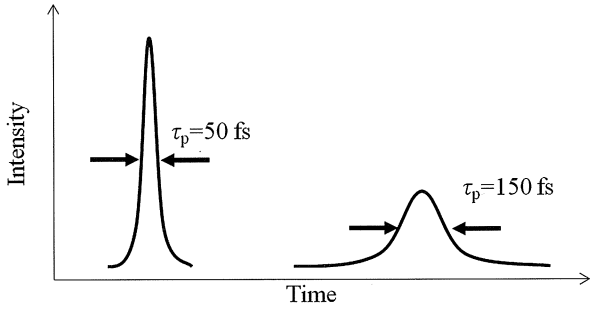

Figure 10 Comparison of peak intensities of laser pulses with the same pulse energy, however with different pulse widths of 50 and 150fs

The fact that a significant difference was seen between a 50fs and 150fs pulse widths for both the trace depth and the sectional area at a wavelength of 800nm means that for the same pulse energy, the processing efficiency improved with increasing peak power, indicates that the processing mechanism is not a simple thermal effect, but rather depends on the instantaneous irradiation power. Figure 10 shows the comparison of peak intensities of laser pulses with the same pulse energy, however with different pulse widths of 50 and 150fs.

5) Effect of sample movement speed and debris removal

In these experiments, because the pulse rate was 1 kHz, at sample movement speeds of 100 and 26μm/s, the number of pulses per unit length differed by a factor of about four. At lower movement speed, the greater the number of pulses per unit length, and the higher the processing rate. In Figure 9, it was seen that both the trace depth and sectional area decreased with increasing movement speed only when an air flow was present. However, that fact that the regression coefficient was not significant was due to one measurement among the three repetitions in this experiment giving an extremely high value. The cause for this is unknown. In considering these results, it is believed that the presence or absence of air has a large effect on processing. Although the sample was mounted vertically on automatic stage,

debris remained. It is suggested that when debris are not removed by an air flow, they remain in the irradiation trace and prevent the sample from receiving sufficient energy for efficient processing. The same phenomenon is seen when processing with mechanical cutting tools, and it has been reported that when cool air is used to remove debris, the cutting force increases and the surface roughness is reduced[36].

6) Evaluation of cavity formation

The average cavity depth was 308.2 ± 11.4μm, the average difference in cavity floor depth (R_{max}) was 37.5 ± 6.8μm, and the average roughness of the cavity floor (R_a) was 4.5 ± 1.5μm. Uno et al. reported the effects that heating CAD/CAM produced ceramic crowns had on the accuracy of the fit[37]. According to this report, R_{max} was 84.8μm before sintering and 58.1μm after sintering. R_a was 4.2μm before sintering and 3.7μm after sintering, the marginal fit was 22.0μm after sintering, and the report concluded that there were no clinical problems. The above values are comparable to those obtained in the present study. McClean and Fraunhofer reported that if the marginal fit was 120μm or less, and Nakamura et al. reported that if the marginal fit was 100μm or less, good clinical results were obtained[38, 39].

In the present study, we processed ceramic blocks in the low power limit of several to 100mW. This was to estimate the best precision available in the processing of ceramics. Hence, it is not realistic to apply the present processing speed to the estimation of the total time for processing ceramic crown and compare it with that using conventional method. For practical application of femtosecond laser to the processing of ceramic crown, we propose the combined use of femtosecond laser with a maximum power of a few W or a nanosecond Nd:YVO_4 laser for rough processing, and those with a low power for fine finishing as we did in the present study. Even as to the processing with femtosecond laser, we have some concrete ideas to improve the processing speed with femtosecond laser. First, we used the femtosecond laser with the duration of 150fs and wavelength at 800nm, owing to the limited machine available time. However, as indicated by the present experimental results, the use of shorter pulse width and wavelength will reduce the processing time of ceramic crown. Second, we could not make use of the full power of laser pulse owing to the formed plasma in air. Hence, processing in vacuum or in gases with higher ionization energy such as noble gases will contribute to the improvement of processing efficiency. To confirm this is one of our future tasks.

Conclusion

Processing of completely-sintered zirconia, semi-sintered zirconia, alumina, and hydroxyapatite was achieved using a femtosecond Ti:sapphire laser. It was found that if water permeated the sample interior, the cutting power increased. In the case of the zirconia samples, darkening of the irradiation traces was observed, but this disappeared when the samples were reheated. The cutting force, as indicated by the depth of the irradiation trace and the sectional area, was found to depend on the irradiation power. It increased rapidly up to a measured beam power of 20mW, and subsequently more slowly. For the same irradiation power, the processing amount increased with decreasing wavelength and pulse width. In addition, it was found that removal of the debris was beneficial for milling. Finally, the surface roughness at the floor of a cavity formed by laser irradiation was determined to be in the clinically applicable range.

The above results suggest that a femtosecond titanium-sapphire laser can be applicable for high-precision processing of dental ceramics.

Acknowledgements

At the completion of this manuscript, we would like to express our deep appreciation regarding this research to Professor Masaaki Ashida, Graduate School of Engineering Science, Osaka University for granting permission to use the laser equipment, confocal microscope, and SEM system, and to Associate professor Masayoshi Ichimiya, School of Engineering, University of Shiga Prefecture for guidance in SEM imaging.

There is no conflict of interest that should be disclosed in regard to this paper.

A summary of this research was published at The 15th Congress of the World Federation for Laser Dentistry (July 17-19, 2016 Nagoya, Japan).

References

1) Yatani H, Miura H, Hosokawa T: Crown and bridge prosthodontics, 5st ed, Tokyo, 2014, Ishiyaku publishers, 282-291.
2) Moriyoshi Y: Inorganic material requisiteness 300, 1st ed, Tokyo, 2008, Sankyo shuppan, 437, 473.
3) Ceramic Society of Japan: Handbook of ceramics, 2nd ed, Tokyo, 2002, Gihodo shuppan, 1146-1149, 1507.
4) Kazama-Koide M, Ohkuma K, Ogura H, et al: A new method for fabricating zirconia coping a Nd:YVO4 nanosecond

laser. Dent Mater J, 33 : 422-429, 2014.
5) Shinya A, Ohsawa J, Kobayashi N, et al: A comparative study on the marginal discrepancies of Full Cast Crowns. J Showa Univ Dent Soc, 15 : 311-314, 1995.
6) Boeckler AF, Stadler A, Setz JM: The significance of marginal gap and overextension measurement in the evaluation of the fit of complete crowns. J Contemp Dent Pract, 6 : 26-37, 2005.
7) Konstantoulakis E, Nakajima H, Woody RD, et al: Marginal fit and surface roughness of crowns made with an accelerated casting technique. J Prosthet Dent, 80 : 337-345, 1998.
8) Christensen GJ: Marginal fit of gold inlay castings. J Prosthet Dent, 16 : 297-305, 1966.
9) Lee KB, Park CW, Kim KH, et al: Marginal and internal fit of all-ceramic crowns fabricated with two different CAD/CAM systems. Dent Mater J, 27 : 422-426, 2008.
10) Miura S, Inagaki R, Kasahara S, et al: Fit of zirconia all-ceramic crowns with different cervical margin designs, before and after porcelain firing and glazing. Dent Mater J, 33 : 484-489, 2014.
11) Suto N, Miura S, Inagaki R: A basic study on fitness of all-ceramic crown fabricated by CAD/CAM system. Ann Jpn Prosthodont Soc, 1 : 21-28, 2009.
12) El-Dessouky RA, Salama MM, Shakal MA, et al: Marginal adaptation of CAD/CAM zirconia-based crown during fabrication steps. Tanta Dental Journal, 12 : 81-85, 2015.
13) Vojdani M, Safari A, Mohaghegh M, et al: The effect of porcelain firing and type of finish line on the marginal fit of zirconia copings. J Dent Shiraz Univ Med Sci, 16 : 113-120, 2015.
14) Farid F, Hajimiragha H, Jelodar R, et al: In vitro evaluation of the effect of core thickness and fabrication stages on the marginal accuracy of an all-ceramic system. Journal of Dentistry, Tehran University of Medical Sciences, 3 : 188-194, 2012.
15) Euán R, Figueras-Álvarez O, Cabratosa-Termes J, et al: Marginal adaptation of zirconium dioxide copings: Influence of the CAD/CAM system and the finish line design. J Prosthet Dent, 112 : 155-162, 2014.
16) Callou TP, Garcia R, Mukai A, et al: Advances in femtosecond laser technology. Clin Ophthalmol, 10 : 697-703, 2016.
17) Nejima R, Terada Y, Mori Y, et al: Clinical utility of femtosecond laser-assisted astigmatic keratotomy after cataract surgery. Jpn J Ophthalmol, 59 : 209-215, 2015.
18) Rego Filho Fde A, Dutra-Corrêa M, Nicolodelli G, et al: Influence of the hydration state on the ultrashort laser ablation of dental hard tissues. Lasers Med Sci, 28 : 215-222, 2013.
19) Ji L, Li L, Devlin H, et al: Ti:sapphire femtosecond laser ablation of dental enamel, dentine, and cementum. Lasers Med Sci, 27 : 197-204, 2012.
20) Uchizono T, Igarashi A, Kato J, et al: Histological observation on dental hard tissue Irradiated by ultra-short pulsed laser. J Jpn Soc Laser Dent, 17 : 81-86, 2006.
21) Murakoshi T, Kobayashi S: Characterization of Mechanical Properties and Bioactibity of Hydroxyapatite/β-Tricalcium Phosphate Composites. Journal of the Japan Society for Composite Materials, 38 : 116-126, 2012.
22) Shiota T, Shibata M, Yasuda K, et al: Influence of β-tricalcium phosphate dispersion on mechanical properties of hydroxyapatite ceramics. Journal of the Ceramic Society of Japan, 116 : 1002-1005, 2008.
23) Furuya Y: Choice of thin HA coated implants. J Bio-Integ, 4 : 85-92, 2014.
24) Kohiga Y, Hatoko Y, Kato N, et al: Preparation and evaluation of fluoridated hydroxyapatite sheets for dentin restoration. DE, 35 : 114, 2016.
25) Hontsu S, Kato N, Yamamoto E, et al: Fabrication of a HA films using the Er:YAG laser. J Bio-Integ, 4 : 65-69, 2014.
26) Tanaka K: Nonlinear Interactions of Laser Light and Plasmas. J Plasma Fusion Res, 81 : 11-18, 2005.
27) Herziger G: The influence of laser-induced plasma on laser material processing the industrial laser annual handbook, Tulsa, PennWell Publishing Company, 108-115, 1986.
28) Nakamura T, Sugano T, Usami H, et al: Fitting accuracy and fracture resistance of crowns using a hybrid zirconia frame made of both porous and dense zirconia. Dent Mater J, 34 : 257-262, 2015.
29) Yoshioka S, Kobayashi T, Tnaka Y, et al: Blackening and crack formation in Q-switched YAG laser machining of zirconia ceramics. J Jpn Soc Prec Eng, 7 : 1277-1282, 1989.
30) Noda M, Okuda Y, Tsuruki, et al: Surface damages of zirconia by Nd:YAG dental laser irradiation. Dent Mater J, 29 : 536-541, 2010.
31) Ban S, Minesaki Y, Takenouchi Y: Blackening and crack formation of zirconia by Nd: YAG laser irradiation. J J Dent Mater, 27 : 181, 2008.
32) Okuda Y, Ban S: Removal method of the zirconia full crown by Nd:YAG laser. Practice in Prosthodontics, 47 : 496-502, 2014.
33) Okuda Y, Ban S, Yoshihara K, et al: Damage of zirconia induced by Nd:YAG dental laser irradiation. Dent Mater J, 33 : 135, 2014.
34) Awazu K: Infrared laser for biomedical engineering, 1st ed, Osaka, 2008, Osaka university press, 54-55.
35) Institute of Electrical Engineers of Japan: Laser ablation and applications, 1st ed, Tokyo, 1999, Corona publishing, 1-4.
36) Hotta M, Wakatuki M, Wago T, et al: Study on turning technique for difficult-to-machine materials of high hardness. Reports of the iwate industrial research institute, 6 : 1-4, 1999.
37) Uno M, Nonogaki R, Yokoyama Y, et al: Effect of heating CAD/CAM-Fabricated ceramic crowns on marginal fit accuracy. Prosthodont Res Prac, 6 : 81-86, 2007.
38) McLean JW, Von Fraunhofer JA: The estimation of cement film thickness by an in vivo technique. Brit Dent J, 131 : 107-111, 1971.
39) Nakamura T, Mutobe Y, Maruyama T: Possibility and present status of all-ceramic crowns state of the art of heat-pressed ceramics. J Jpn Prosthodont Soc, 43 : 217-224, 1999.